

Energy & Environmental Science

Accepted Manuscript



This is an *Accepted Manuscript*, which has been through the Royal Society of Chemistry peer review process and has been accepted for publication.

Accepted Manuscripts are published online shortly after acceptance, before technical editing, formatting and proof reading. Using this free service, authors can make their results available to the community, in citable form, before we publish the edited article. We will replace this *Accepted Manuscript* with the edited and formatted *Advance Article* as soon as it is available.

You can find more information about *Accepted Manuscripts* in the [Information for Authors](#).

Please note that technical editing may introduce minor changes to the text and/or graphics, which may alter content. The journal's standard [Terms & Conditions](#) and the [Ethical guidelines](#) still apply. In no event shall the Royal Society of Chemistry be held responsible for any errors or omissions in this *Accepted Manuscript* or any consequences arising from the use of any information it contains.

COMMUNICATION

Band engineering of high performance p-type FeNbSb based half-Heusler thermoelectric materials for figure of merit $zT > 1$

Cite this: DOI: 10.1039/x0xx00000x

Received 00th January 2012,
Accepted 00th January 2012Chenguang Fu,^a Tiejun Zhu,^{*ab} Yintu Liu,^a Hanhui Xie^a and Xinbing Zhao^{ab}

DOI: 10.1039/x0xx00000x

www.rsc.org/ees

We report new p-type FeNb_{1-x}Ti_xSb (0.04 ≤ x ≤ 0.24) half-Heusler thermoelectric materials with a maximum zT of 1.1 at 1100K, which is twice higher than the ZrCoSb half-Heusler alloys. The electrical properties are optimized by a tradeoff between band effective mass and mobility via a band engineering approach. High content of Ti up to $x=0.2$ optimizes the power factor and reduces lattice thermal conductivity. In view of abundantly available elements, good stability and high zT , FeNb_{1-x}Ti_xSb alloys can be great promising for high temperature power generation.

Thermoelectric (TE) materials allow for direct thermal-to-electric energy conversion without hazardous liquids, moving parts, or green house emissions. The demand for new sustainable energy technology, the environmental concern for use of fossil fuel, and the ubiquitous heat source have consistently driven the pursuit of higher performance TE materials.¹ The conversion efficiency of a TE device strongly depends on the materials' dimensionless figure of merit zT , $zT = \alpha^2 \sigma T / (\kappa_e + \kappa_L)$, where α , σ , T , κ_e and κ_L are respectively the Seebeck coefficient, the electrical conductivity, the absolute temperature, and the electron and lattice components of total thermal conductivity κ .² Developing bulk materials with high zT is the central theme for the large scale application of TE technology. Up to now, Bi₂Te₃-based materials are the most efficient for refrigeration near room temperature,³ PbTe, filled skutterudites and Mg₂(Si,Sn) are promising for mid-temperature power generation,^{4,7} and SiGe and Yb₁₄MnSb₁₁ are known for high-temperature TE application.^{8,9}

Half-Heusler (HH) compounds, with a valence electron count of 8 or 18, have recently been identified as one of most promising TE materials for high temperature power generation due to their excellent electrical and mechanical properties and high temperature stability.¹⁰⁻¹⁴ The n-type (Zr,Hf)NiSn based HH compounds have exhibited the maximum zT as high as ~1.0 at 1000K, which exceeds

the industry benchmark set by SiGe high temperature alloys ($zT \sim 0.8$ for n-type and 0.6 for p-type).¹⁰⁻¹⁴ However, the typical p-type HH compounds, (Zr,Hf)CoSb, have the reproducible highest zT of only ~0.5.^{10,14} Therefore, developing high performance p-type HH compounds is imperative to achieve high efficiency high temperature TE devices based on HH compounds, because the practical systems require both n- and p-type materials with similar properties.¹⁰

FeVSb based HH compounds with abundantly available constituent elements, despite of high power factor $\alpha^2 \sigma$ ($\sim 4.5 \times 10^{-3} \text{ Wm}^{-1} \text{ K}^{-2}$ at 300K), have been paid less attention due to its high lattice thermal conductivity ($\sim 10 \text{ Wm}^{-1} \text{ K}^{-1}$ at 300K) and low zT (~ 0.3 for n-type).^{15,16} In our previous study, a significantly reduced thermal conductivity of $5.5 \text{ Wm}^{-1} \text{ K}^{-1}$ at 300K was obtained for the FeV_{0.6}Nb_{0.4}Sb solid solutions by the enhanced point defect scattering of phonons.¹⁶ Fe(V,Nb)Sb solid solutions can be promising p-type TE materials due to the high band degeneracy and the reduced lattice thermal conductivity. However, there are two factors hindering the further improvement of the alloys' TE performance: One is the optimal carrier concentration can not be reached due to the limited solubility of Ti dopant on V/Nb sites; the other is the low carrier mobility leads to a relatively low power factor ($\sim 3.0 \times 10^{-3} \text{ Wm}^{-1} \text{ K}^{-2}$ at 900K).¹⁵

If acoustic phonon scattering dominates the carrier transport, the $zT \propto N_v / m_b^* \kappa_L$,¹⁷ where N_v is the number of degenerate valleys and m_b^* is band effective mass. This suggests that multiple degenerate valleys with low band effective mass and low lattice thermal conductivity are beneficial for high zT .^{4,5,18,19} In fact, most of recent work on enhancing zT have been focused on two strategies: one is to reduce the lattice thermal conductivity κ_L by alloying or nanostructuring to enhance phonon scattering,^{1,5,20,21} the other is to improve the electrical properties by band engineering, such as band convergence^{4,22} or resonant states.²³

P-type Fe(V,Nb)Sb HH solid solutions have high band degeneracy and relatively low lattice thermal conductivity.¹⁵ Therefore, further enhancement of the zT may be realized by reducing the band effective mass to improve the mobility. Generally, the heavier band gives a larger band effective mass. Electronic band calculation shows the valence band maximums (VBMs) of both FeVSb and FeNbSb locate at L point with twofold orbital degeneracy,^{24,25} and the valence band of FeVSb are flatter than FeNbSb.²⁴ Therefore, increasing Nb content in the Fe(V_{1-y}Nb_y)Sb solid solutions may achieve lower valence band effective mass and consequently higher carrier mobility. Moreover, the decrease in band effective mass can lead to the decrease in optimal carrier concentration,¹⁸ which is favorable for p-type Fe(V,Nb)_{1-x}Ti_xSb due to the limited solubility of Ti.¹⁵ Furthermore, FeNbSb has larger band gap E_g (~0.54eV) than that of FeVSb (~0.34eV),^{15,25} and increasing Nb content in Fe(V_{1-y}Nb_y)_{1-x}Ti_xSb will prevent the degradation of the TE performance at high temperatures due to the thermally activated minority carriers.

In this work, we indeed obtain a high zT of 1.1 at 1100K for FeNb_{1-x}Ti_xSb without V substitution, which is the highest reported value for p-type HH compounds. The decreased band effective mass and the increased band gap with increasing Nb content in Fe(V_{1-y}Nb_y)_{1-x}Ti_xSb lead to the enhanced carrier mobility and the diminished bipolar conduction at high temperature respectively, and high content of Ti doping not only optimizes the carrier concentration but also guarantees the reduced lattice thermal conductivity in FeNb_{1-x}Ti_xSb (0.04 ≤ x ≤ 0.24), which all contribute to the high zT , demonstrating that p-type FeNb_{1-x}Ti_xSb alloys are promising TE materials for high temperature power generation.

Electronic band structures of FeVSb and FeNbSb have been investigated by the first principles calculations (Fig. S1, ESI) and our results are similar to previously reported.^{24,25} The valence band of FeVSb is flatter than FeNbSb, indicating that increasing Nb content in Fe(V_{1-y}Nb_y)_{1-x}Ti_xSb will lead to a lower band effective mass (Table S1, ESI).

The carrier concentration dependence of Seebeck coefficient for Fe(V_{1-y}Nb_y)_{1-x}Ti_xSb samples at room temperature is shown in Fig. 1(a), which agrees well with the calculated curves using a single parabolic band (SPB) model.¹² A distinct decrease of band effective mass m_b^* can be found with increasing Nb content y , varying from 2.5 m_e for p-type Fe(V_{0.6}Nb_{0.4})_{1-x}Ti_xSb to 1.6 m_e for FeNb_{1-x}Ti_xSb. Unchanged band effective mass with increasing Ti content in Fe(V_{1-y}Nb_y)_{1-x}Ti_xSb samples indicate that substituting Ti at V/Nb sites has no effect on valence band structure. This can be understood from the fact that the valence band structure is dominated by the electronic character of Fe element (Fig. S1, ESI), and is also consistent with the previous results by Jodin *et al.*²⁵

The decrease in m_b^* is beneficial for the increase of carrier mobility. As shown in Fig. 1(b), the carrier mobility of FeNb_{1-x}Ti_xSb is twice as high as that of Fe(V_{0.6}Nb_{0.4})_{1-x}Ti_xSb. The room temperature carrier mobility of FeNb_{1-x}Ti_xSb are about 15-25cm²V⁻¹s⁻¹, which are higher than that of the other Fe-containing p-type TE

materials.^{26,27} For example, the carrier mobility of p-type FeVSb is about 1-4cm²V⁻¹s⁻¹,²⁶ while p-type Fe-based skutterudites have the carrier mobility of ≤10cm²V⁻¹s⁻¹.²⁷ The low mobility in these Fe-containing p-type TE materials is due to the heavy band mass resulting from the spatially localized nature of transition metal 3d orbitals.²⁸ In addition to the decrease in m_b^* , the reduced alloy scattering of carriers should also contribute to the increased carrier mobility in p-type FeNb_{1-x}Ti_xSb, compared to Fe(V_{0.6}Nb_{0.4})_{1-x}Ti_xSb solid solutions.

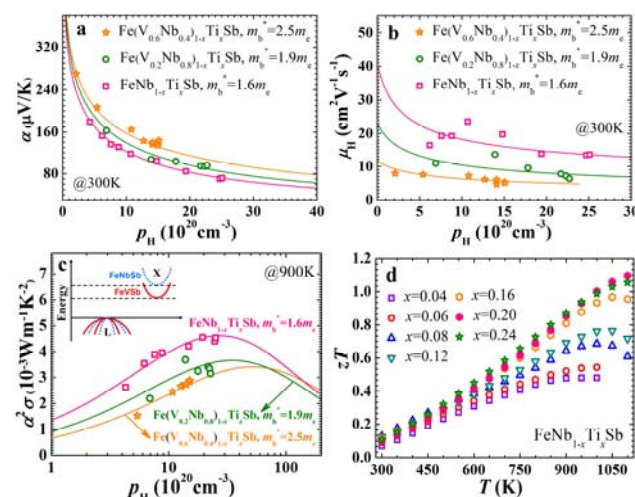


Fig. 1 (a) Seebeck coefficient versus the Hall carrier concentration for Fe(V_{1-y}Nb_y)_{1-x}Ti_xSb samples at 300K. (b) Mobility versus carrier concentration for the samples at 300K. (c) Carrier concentration dependence of power factor at 900K. The inset in (c) shows schematic representation of valence and conduction band structure of FeVSb (red solid line) and FeNbSb (blue dot line). (d) Temperature dependence of zT of FeNb_{1-x}Ti_xSb samples. The theoretical curves (solid lines) were calculated by SPB model.

The decreased m_b^* leads to the low Seebeck coefficient but contributes more to the enhanced carrier mobility. As a result, the optimal power factor distinctly increases with decreasing m_b^* (Fig. 1(c)), while the optimal carrier concentration p_{opt} decreases with the decreased m_b^* . For FeNb_{1-x}Ti_xSb system, the p_{opt} is ~2.6 × 10²¹ cm⁻³, lower than that of the Fe(V_{1-y}Nb_y)_{1-x}Ti_xSb solid solutions. In Fe(V_{0.6}Nb_{0.4})_{1-x}Ti_xSb, the experimentally obtained maximum carrier concentration is only ~1.5 × 10²¹ cm⁻³ due to the limited solubility of Ti, far below the p_{opt} of ~6 × 10²¹ cm⁻³.¹⁵ Decreasing m_b^* makes it possible to achieve the optimal power factor at lower carrier concentration in FeNb_{1-x}Ti_xSb system. Similar phenomenon is also found in high performance PbTe system.¹⁸

Therefore, the TE properties of p-type Ti doped FeNb_{1-x}Ti_xSb ($x = 0.04 \sim 0.24$) alloys were systematically investigated. Fig. 1(d) indeed shows that the zT of FeNb_{1-x}Ti_xSb samples increases with increasing Ti content and a very high zT of 1.1 is reached at 1100K for FeNb_{0.8}Ti_{0.2}Sb, which is the highest reported value for p-type HH compounds.

The transport features of $\text{FeNb}_{1-x}\text{Ti}_x\text{Sb}$ were discussed in detail below. The electrical conductivity of $\text{FeNb}_{1-x}\text{Ti}_x\text{Sb}$ samples decreases rapidly above room temperature and follow a temperature dependence of $T^{-1.5}$ (Fig. 2(a)), implying the acoustic phonon scattering dominated charge transport,²⁹ since the hole concentration is almost independent of temperature before intrinsic excitation for heavily doped semiconductors¹⁵ (Fig. S2, ESI). The calculated Seebeck coefficient α by the SPB model, in Fig. 2(b), agrees well with the experimental data before the intrinsic excitation of charge carriers. All the $\text{FeNb}_{1-x}\text{Ti}_x\text{Sb}$ samples have high power factors PF (Fig. S3, ESI), and the PF of p-type $\text{FeNb}_{0.8}\text{Ti}_{0.2}\text{Sb}$ is about $4.5 \times 10^{-3} \text{ W m}^{-1} \text{ K}^{-2}$ at 1100K, comparable with that of the optimized n-type (Hf,Zr)NiSn based HH compounds,¹¹ and about twice as high as that of the most widely used p-type SiGe alloys for high temperature power generation.³⁰

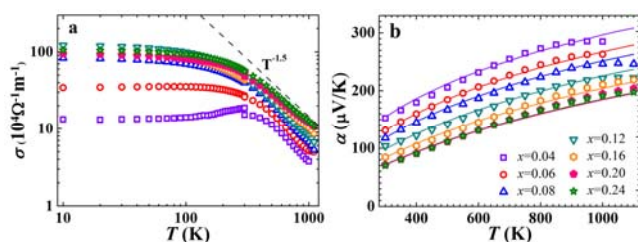


Fig. 2 Temperature dependence of electrical conductivity (a) and Seebeck coefficient (b) for $\text{FeNb}_{1-x}\text{Ti}_x\text{Sb}$ samples. The theoretical curves in (b) were calculated under SPB model.

The temperature dependence of thermal conductivity κ and lattice thermal conductivity κ_L of $\text{FeNb}_{1-x}\text{Ti}_x\text{Sb}$ alloys are shown in Fig. 3. The lattice thermal conductivity was obtained by subtracting the electronic component κ_e from the total thermal conductivity κ . κ_e was calculated via $\kappa_e = L\sigma T$, where L is the Lorenz number and can be calculated under the SPB model with the reasonable approximation.¹² The total thermal conductivity at room temperature decreases from $15 \text{ W m}^{-1} \text{ K}^{-1}$ at $x=0.04$ to $7.5 \text{ W m}^{-1} \text{ K}^{-1}$ at $x=0.2$, mainly resulting from the significant decrease in the lattice thermal conductivity (Fig. 3(b)). The κ_L decreases rapidly with increasing Ti content over the measured temperature, indicating that the substitution of Ti at Nb sites is an effective way to reduce the κ_L of FeNbSb . The lattice thermal conductivity of all $\text{FeNb}_{1-x}\text{Ti}_x\text{Sb}$ samples follows a $\kappa_L \sim T^s$ behavior with the exponent $-0.5 \leq s < -1$, indicating the strong point defect scattering is present.³¹

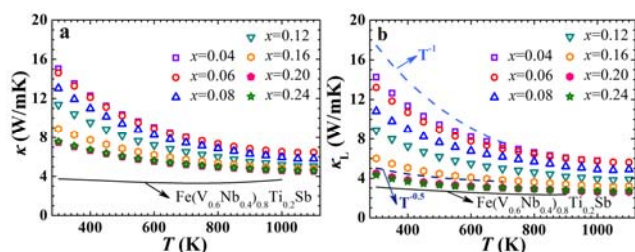


Fig. 3 Thermal conductivity κ (a) and Lattice thermal conductivity κ_L (b) of $\text{FeNb}_{1-x}\text{Ti}_x\text{Sb}$ samples. The solid lines in (a) and (b) show the κ and κ_L of $\text{Fe}(\text{V}_{0.6}\text{Nb}_{0.4})_{0.8}\text{Ti}_{0.2}\text{Sb}$ for comparison.

Although p-type $\text{FeNb}_{1-x}\text{Ti}_x\text{Sb}$ have the largest power factor among $\text{Fe}(\text{V}_{1-y}\text{Nb}_y)_{1-x}\text{Ti}_x\text{Sb}$ alloys, they have the higher lattice thermal conductivity compared with the V substituted solid solutions due to the stronger point defect scattering of phonons in the latter.¹⁶ However, the room temperature κ_L of $\text{FeNb}_{1-x}\text{Ti}_x\text{Sb}$ samples rapidly decreases with increasing Ti content (Fig. S4a, ESI), and are only $\sim 30\%$ higher than the $\text{Fe}(\text{V}_{0.6}\text{Nb}_{0.4})_{1-x}\text{Ti}_x\text{Sb}$ solid solutions at high Ti contents ($x \geq 0.2$). At higher temperatures, due to the strong phonon-phonon scattering, the difference in κ_L between $\text{FeNb}_{0.8}\text{Ti}_{0.2}\text{Sb}$ and the $\text{Fe}(\text{V}_{0.6}\text{Nb}_{0.4})_{0.8}\text{Ti}_{0.2}\text{Sb}$ is even smaller, only $\sim 15\%$ at 800K (Fig. S4b, ESI). Calculations of phonon relaxation time using Callaway model reveals that in $\text{FeNb}_{0.8}\text{Ti}_{0.2}\text{Sb}$ the Umklapp process is dominant at 400K (Fig. S5, ESI).³² Although it was previously reported that the low content Ti could improve the electrical conductivity in $\text{FeNb}_{0.95}\text{Ti}_{0.05}\text{Sb}$,²⁴ our work firstly shows high content Ti doping at Nb sites not only optimizes the carrier concentration but also enhances the point defect scattering of phonons to suppress the lattice thermal conductivity.

It is noteworthy that the band gap of $\text{FeNb}_{1-x}\text{Ti}_x\text{Sb}$ ($\sim 0.54 \text{ eV}$) is larger than that of $\text{Fe}(\text{V}_{0.6}\text{Nb}_{0.4})_{1-x}\text{Ti}_x\text{Sb}$ ($\sim 0.42 \text{ eV}$), which is beneficial to inhibit the intrinsic excitation of minority carrier and leads to the maximum Seebeck coefficient occurs at higher temperature (Fig. S6, ESI). The thermal conductivity of $\text{Fe}(\text{V}_{0.6}\text{Nb}_{0.4})_{0.8}\text{Ti}_{0.2}\text{Sb}$ begins to increase above 800K due to the bipolar conduction, whereas in $\text{FeNb}_{1-x}\text{Ti}_x\text{Sb}$ it is above 1100K (Fig. (3)). Therefore, the increased band gap and suppressed bipolar conduction also contribute to the high zT at high temperature in $\text{FeNb}_{1-x}\text{Ti}_x\text{Sb}$.

As shown in Fig. 1(d), $\text{FeNb}_{1-x}\text{Ti}_x\text{Sb}$ alloys exhibit a maximum zT of 1.1 at $x=0.2$. Compared with other good p-type high temperature TE materials (Fig. (4)), $\text{FeNb}_{0.8}\text{Ti}_{0.2}\text{Sb}$ is more competitive in high temperature power generation. Especially, the maximum zT of $\text{FeNb}_{0.8}\text{Ti}_{0.2}\text{Sb}$ half-Heusler alloy is almost twice as high as that of the most widely used p-type SiGe TE materials.³⁰ At high temperatures ($>900 \text{ K}$) the p-type $\text{FeNb}_{0.8}\text{Ti}_{0.2}\text{Sb}$ displays superior TE performance to the optimized n-type (Hf,Zr)NiSn compound, which makes it possible to achieve a high efficiency TE device based on half-Heusler alloys. The good experimental repeatability and high temperature stability of $\text{FeNb}_{0.8}\text{Ti}_{0.2}\text{Sb}$ have also been confirmed (Figs. 7 and 8, ESI).

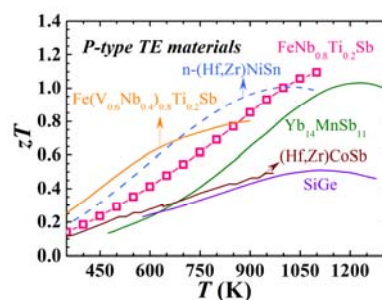


Fig. 4 zT comparison for typical high temperature p-type TE materials. TE performance of $\text{FeNb}_{0.8}\text{Ti}_{0.2}\text{Sb}$ superior to other advanced high temperature p-type materials (solid line)^{9,14,15,30} and the optimized n-type (Hf,Zr)NiSn¹¹ based HH compound (dash line).

In summary, the new high performance p-type FeNb_{1-x}Ti_xSb half-Heusler thermoelectric alloys were developed via a band engineering approach through a tradeoff between band effective mass and carrier mobility. A high zT value of 1.1 at 1100K was achieved for FeNb_{0.8}Ti_{0.2}Sb. High content of Ti doping at Nb sites not only optimizes the power factor but also enhances point defect scattering of phonons. The increased band gap of FeNb_{1-x}Ti_xSb, compared to Fe(V_{0.6}Nb_{0.4})_{1-x}Ti_xSb, leads to the suppressed intrinsic excitation at high temperatures. Considering the competitive cost, good stability and high TE properties, FeNb_{1-x}Ti_xSb alloys exhibit bright potential for high temperature TE power generation.

Methods

Synthesis. The ingots (~20g) with nominal composition Fe(V_{1-y}Nb_y)_{1-x}Ti_xSb ($x = 0\sim 0.24$, $y=0.4\sim 1.0$) were prepared by levitation melting of stoichiometric amount of Fe (piece, 99.97%), V (piece, 99.97%), Nb (foil, 99.98%), Ti (rod, 99.99%) and Sb (block, 99.999%) under an argon atmosphere for 3 minutes. The ingots were remelted three times to ensure homogeneity. The obtained ingots were mechanical milled (Mixer Mill MM200, Retsch) for 4h under argon protection. The obtained powders were loaded into the graphite die and compacted by spark plasma sintering (SPS-1050, Sumitomo Coal Mining Co.) at 1123 K for 10 min under 65 MPa in vacuum. The as-sintered samples, of which the relative densities were found to be ~95%, were annealed at 1023 K for 2 days.

Structural characterization. Phase structures of the samples were investigated by X-ray diffraction (XRD) on a RigakuD/MAX-2550PC diffractometer using Cu K_α radiation ($\lambda_0=1.5406$ Å) and the chemical compositions were checked by electron probe microanalysis (EPMA, JEOL, JXA-8100). The XRD patterns of Fe(V_{1-y}Nb_y)_{1-x}Ti_xSb show a single phase that can be indexed to the HH phase with a cubic MgAgAs-type crystal structure (space group, F43m),¹⁵ and the XRD patterns of FeNb_{1-x}Ti_xSb ($x = 0\sim 0.24$) samples are given in Fig. S9a. The lattice parameters of FeNb_{1-x}Ti_xSb were calculated via Bragg's law using Jade® codes, which decrease almost linearly with the nominal Ti content (Fig. S9b, ESI) since the covalent radius of Ti is smaller than that of Nb. The fairly good linearity is consistent with the Vegard's law. The microstructure and homogeneity of FeNb_{0.8}Ti_{0.2}Sb were investigated by EPMA (Fig. S10, ESI). The EPMA results (Table S2, ESI) show that the actual compositions are close to the nominal ones.

TE property measurement. The low temperature electrical conductivity and Hall coefficients from 10K to 300K were measured using a Mini Cryogen Free Measurement System (Cryogenic Limited, UK). The carrier concentration p_H was calculated by $p_H = 1/eR_H$, where e is the unit charge and R_H is the Hall coefficient. The carriers mobility μ_H was calculated by $\mu_H = \sigma R_H$. The Seebeck coefficient and electrical conductivity from 300K-1100K were measured on a commercial Linseis LSR-3 system using a differential voltage/temperature technique and a DC four-probe method. The thermal conductivity κ was calculated by using $\kappa = D\rho C_p$, where ρ is the sample density estimated by the Archimedes method. The thermal diffusivity D and specific heat C_p were measured by a laser flash method on Netzsch LFA457 instrument with a Pyroceram

standard (Fig. S11, ESI). The accuracy is $\pm 3\%$ and $\pm 5\%$, respectively.

Acknowledgments

The work was supported by the National Basic Research Program of China (2013CB632503), the Nature Science Foundation of China (51171171), the Program for New Century Excellent Talents in University (NCET-12-0495), the Program for Innovative Research Team in University of Ministry of Education of China (IRT13037), and the Ph.D program Foundation of Ministry of Education of China (No. 20120101110082).

Notes and references

^a State Key Laboratory of Silicon Materials and Department of Materials Science and Engineering, Zhejiang University, Hangzhou 310027, China E-mail: zhutj@zju.edu.cn

^b Key Laboratory of Advanced Materials and Applications for Batteries of Zhejiang Province, Zhejiang University, Hangzhou 310027, China.

Electronic Supplementary Information (ESI) available: [Band structure calculation, electrical and thermal properties, Thermogravimetric analysis, Reproducibility, XRD patterns, Electron probe microanalysis]. See DOI: 10.1039/c000000x/

- L. D. Zhao, V. P. Dravid and M. G. Kanatzidis, *Energy Environ. Sci.*, 2014, **7**, 251.
- G. J. Snyder and E. S. Toberer, *Nature Mater.*, 2008, **7**, 105.
- B. Poudel, Q. Hao, Y. Ma, Y. Lan, A. Minnich, B. Yu, X. Yan, D. Wang, A. Muto, D. Vashaee, X. Chen, J. Liu, M. S. Dresselhaus, G. Chen and Z. Ren. *Science*, 2008, **320**, 634.
- Y. Z. Pei, X. Y. Shi, A. Lalonde, H. Wang, L. D. Chen and G. J. Snyder, *Nature*, 2011, **473**, 66.
- K. Biswas, J. He, I. D. Blum, C. I. Wu, T. P. Hogan, D. N. Seidman, V. P. Draid and M. G. Kanatzidis, *Nature*, 2012, **489**, 414.
- X. Shi, J. Yang, J. R. Salvador, M. Chi, J. Y. Cho, H. Wang, S. Bai, J. H. Yang, W. Q. Zhang and L. D. Chen, *J. Am. Chem. Soc.*, 2011, **133**, 7837.
- G. Y. Jiang, J. He, T. J. Zhu, C. G. Fu, X. H. Liu, L. P. Hu and X. B. Zhao, *Adv. Funct. Mater.*, 2014, **24**, 3776.
- C. B. Vining, W. Laskow, J. O. Hanson, R. R. Van der Beck and P. D. Gorsuch, *J. Appl. Phys.*, 1991, **69**, 331.
- S. R. Brown, S. M. Kauzlarich, F. Gascoin and G. J. Snyder, *Chem. Mater.*, 2006, **18**, 1873.
- W. Xie, A. Weidenkaff, X. Tang, Q. Zhang, J. Poon and T. M. Tritt, *Nanomaterials*, 2012, **2**, 379.
- C. Yu, T. J. Zhu, R. Z. Shi, Y. Zhang, X. B. Zhao and J. He, *Acta Mater.*, 2009, **57**, 2757.
- H. H. Xie, H. Wang, Y. Z. Pei, C. G. Fu, X. H. Liu, G. J. Snyder, X. B. Zhao and T. J. Zhu, *Adv. Funct. Mater.*, 2013, **23**, 5123.
- M. Schwall and B. Balke, *Phys. Chem. Chem. Phys.*, 2013, **15**, 1868.
- S. R. Culp, J. W. Simonson, S. J. Poon, V. Ponnambalam, J. Edwards and T. M. Tritt, *Appl. Phys. Lett.*, 2008, **93**, 022105.
- C. G. Fu, T. J. Zhu, Y. Z. Pei, H. H. Xie, H. Wang, G. J. Snyder, Y. Liu, Y. T. Liu and X. B. Zhao, *Adv. Energy Mater.*, DOI: 10.1002/aenm.201400600.

- 16 C. G. Fu, H. H. Xie, T. J. Zhu, J. Xie and X. B. Zhao, *J. Appl. Phys.*, 2012, **112**, 124915.
- 17 Y. Z. Pei, H. Wang and G. J. Snyder, *Adv. Mater.*, 2012, **24**, 6125.
- 18 Y. Z. Pei, A. D. Lalonde, H. Wang and G. J. Snyder, *Energy Environ. Sci.*, 2012, **5**, 7963.
- 19 M. Zhou, Z. M. Gibbs, H. Wang, Y. Han, C. Xin, L. Li and G. J. Snyder, *Phys. Chem. Chem. Phys.*, 2014, **16**, 20741.
- 20 J. F. Li, W. S. Liu, L. D. Zhao and M. Zhou, *NPG Asia Mater.*, 2010, **2**, 152.
- 21 J. Yang, G. P. Meisner and L. Chen, *Appl. Phys. Lett.*, 2004, **85**, 1140.
- 22 L. D. Zhao, H. J. Wu, S. Q. Hao, C. I. Wu, X. Y. Zhao, K. Biswas, J. Q. He, T. P. Hogan, C. Uher, C. Wolverton, V. P. Dravid and M. G. Kanatzidis, *Energy Environ. Sci.*, 2013, **6**, 3346.
- 23 J. P. Heremans, V. Jovovic, E. S. Toberer, A. Saramat, K. Kurosaki, A. Charoenphakdee, S. Yamanaka and G. J. Snyder, *Science*, 2008, **321**, 554.
- 24 D. P. Young, P. Khalifah, R. J. Cava and A. P. Ramirez, *J. Appl. Phys.*, 2000, **87**, 317.
- 25 L. Jodin, J. Tobola, P. Pecheur, H. Scherrer and S. Kaprzyk, *Phys. Rev. B*, 2004, **70**, 184207.
- 26 M. Zou, J. F. Li and T. Kita, *J. Solid State Chem.*, 2013, **198**, 125.
- 27 P. F. Qiu, J. Yang, R. H. Liu, X. Shi, X. Y. Huang, G. J. Snyder, W. Zhang and L. D. Chen, *J. Appl. Phys.*, 2011, **109**, 063713.
- 28 J. Yang, P. Qiu, R. Liu, L. Xi, S. Zhang, W. Zhang, L. Chen, D. J. Singh and J. H. Yang, *Phys. Rev. B*, 2011, **84**, 235205.
- 29 X. Shi, Y. Z. Pei, G. J. Snyder and L. Chen, *Energy Environ. Sci.*, 2011, **4**, 4086.
- 30 C. B. Vining, W. Laskow, J. O. Hanson, R. R. Van der Beck and P. D. Gorsuch, *J. Appl. Phys.*, 1991, **69**, 4333.
- 31 P. G. Klemens, *Phys. Rev.*, 1960, **119**, 507.
- 32 J. Callaway, *Phys. Rev.*, 1959, **113**, 1046.